


The effect of residual palladium on the performance of organic electrochemical transistors

Received: 4 July 2022

Accepted: 12 December 2022

Published online: 27 December 2022

 Check for updates

Sophie Griggs¹, Adam Marks¹, Dilara Meli², Gonzague Rebetez³, Olivier Bardagot³, Bryan D. Paulsen⁴, Hu Chen^{5,6}, Karrie Weaver⁷, Mohamad I. Nugraha^{8,9}, Emily A. Schafer⁴, Joshua Tropp⁴, Catherine M. Aitchison¹, Thomas D. Anthopoulos⁸, Natalie Banerji³, Jonathan Rivnay^{4,10} & Iain McCulloch^{1,5} ✉

Organic electrochemical transistors are a promising technology for bioelectronic devices, with applications in neuromorphic computing and healthcare. The active component enabling an organic electrochemical transistor is the organic mixed ionic-electronic conductor whose optimization is critical for realizing high-performing devices. In this study, the influence of purity and molecular weight is examined for a p-type polythiophene and an n-type naphthalene diimide-based polymer in improving the performance and safety of organic electrochemical transistors. Our preparative GPC purification reduced the Pd content in the polymers and improved their organic electrochemical transistor mobility by ~60% and 80% for the p- and n-type materials, respectively. These findings demonstrate the paramount importance of removing residual Pd, which was concluded to be more critical than optimization of a polymer's molecular weight, to improve organic electrochemical transistor performance and that there is readily available improvement in performance and stability of many of the reported organic mixed ionic-electronic conductors.

Organic mixed ionic-electronic conductors (OMIECs) are materials capable of conducting both ionic and electronic charge carriers, and operate via volumetric-electronic coupling rather than an interfacial regime¹. These properties enable efficient charge storage and signal transduction, making OMIECs applicable to a plethora of applications, including thermoelectric generators^{2,3}, actuators^{4,5}, inverters⁶, sensors^{7–9}, light-emitting electrochemical cells^{10,11}, and batteries^{12–14}.

OMIECs are also employed as the channel material in organic electrochemical transistors (OECTs) on account of their low operational voltages and ability to transduce and amplify an ionic signal into a readable electronic output¹⁵. This, combined with the biological compatibility conferred by organic materials, renders OECTs a promising technology for sensing applications in healthcare settings¹⁶, as well as in neuromorphic computing^{17,18}.

¹Department of Chemistry, Chemistry Research Laboratory, University of Oxford, Oxford OX1 3TA, UK. ²Department of Materials Science and Engineering, Northwestern University, Evanston, IL 60208, USA. ³Department of Chemistry, Biochemistry and Pharmaceutical Sciences (DCBP), University of Bern, Freiestrasse 3, 3012 Bern, Switzerland. ⁴Department of Biomedical Engineering, Northwestern University, Evanston, IL 60208, USA. ⁵KAUST Solar Center (KSC), King Abdullah University of Science and Technology (KAUST), Thuwal 23955-6900, Saudi Arabia. ⁶Great Bay University, 523808 Dongguan, China. ⁷Department of Earth System Science, Stanford University, Stanford, CA 94305, USA. ⁸Physical Sciences and Engineering Division (PSE), KAUST Solar Center (KSC), King Abdullah University of Science and Technology (KAUST), Thuwal 23955-6900, Saudi Arabia. ⁹Research Center for Advanced Materials, National Research and Innovation Agency (BRIN), South Tangerang, Banten 15314, Indonesia. ¹⁰Simpson Querrey Institute, Northwestern University, Chicago, IL 60611, USA. ✉e-mail: iain.mcculloch@chem.ox.ac.uk

Typically, OECTs are comprised of an OMIEC channel, separating a source and a drain electrode, coupled to a gate electrode through an electrolyte (Supplementary Fig. 1). Application of a gate voltage (V_g) drives ions from the electrolyte into the OMIEC. These compensate electronic charges in the channel, which in turn modulates the OMIEC channel conductivity. Channel currents driven by an applied source-drain bias are sensitive to the gate-induced channel conductance modulation, thus allowing for gate signals to be transduced and amplified. This difference between the three-dimensional nature of OECTs and the interfacial operation of organic thin film transistors (OTFTs)¹⁹ presents new challenges to current understanding and indicates that previous assumptions on the similarity of OTFTs and OECTs may not hold true³.

The performance of OECT devices is typically evaluated by examining the steady-state electrical performance, which can be represented by the maximum transconductance (g_m) achieved in devices, calculated from:

$$g_m = \mu C^* \frac{Wd}{L} (V_{TH} - V_g) \quad (1)$$

where μ is the electronic charge carrier mobility, C^* is the volumetric capacitance, W , d , and L are the channel width, depth and length respectively, V_{TH} is the threshold voltage and V_g is the gate voltage²⁰. Transconductance is a direct measure of an OECT's ability to amplify a signal, which can be critical for certain applications, such as in bio-sensing, where a small ionic fluctuation can be transduced into a larger, readable electronic output. Equation (1) highlights the dependence of g_m on both material properties (μC^*) and device geometry (Wd/L). As an alternative figure-of-merit to g_m for understanding the performance of an OECT and to allow for direct material comparisons, the product μC^* is commonly employed instead, to eliminate geometry dependence²¹. Other important parameters when considering the application of an OECT include the ON/OFF ratio and the switching speed. The ON/OFF ratio, similar to an OFET, refers to the ratio of the maximum I_d recorded at a particular V_D , and the I_d measured in the OFF state. Ideal transistors exhibit a low ON resistance and extremely high OFF resistance, which result in a high ON/OFF ratio. A low number (i.e., a high OFF current) is indicative of current leakage or ambient doping of the semiconductor material. Alternatively, a low mobility (i.e., a low ON current) would also result in a low ON/OFF ratio, thus maximizing the charge carrier mobility is critical for meaningful device applications beyond achieving the highest possible μC^* . The switching speed is also critical when considering oscillations in brain activity, for example, which can occur on frequencies in the range of 0.5–200 Hz^{15,22}. Currently, OECTs are able to achieve switching speeds in the microsecond timescales.

One factor that has been demonstrated to influence the performance of organic semiconducting polymers is the molecular weight. Typically in the field of organic transistors and molecular weight studies, the number average molecular weight, M_n is the most widely reported^{23–28}. M_n is defined as the total weight of the polymer divided by the total number of polymer chains, and the dispersity (\mathcal{D}) is a measure of the distribution of the molecular weight within a sample, with a \mathcal{D} of one being optimal and indicating all polymer chains are of equal length. Information on the methods of measuring molecular weight and their respective advantages and limitations are detailed in the Supplementary Information.

Many studies have been carried out on the relationship between charge carrier mobility in OTFTs and the molecular weight of the organic semiconducting layer, arising from mainly morphological factors^{29–33}. Less is known about the influence of molecular weight in OECT devices that mostly differ from OTFTs by the swelling and bulk

doping of the active layer due to ion penetration/expulsion. The dependence of OTFT performance on the molecular weight of the active semiconductor has typically focused on poly(3-hexylthiophene) (P3HT), where both individual batches and blends of different molecular weights have been examined^{30,31,33,34}. Longer polymer chains, occurring in higher molecular weight batches, act as tie chains, connecting crystalline domains and maximizing charge carrier mobilities. This was confirmed by blending low and high molecular weight batches of P3HT in varying percentages, until a plateau was reached in the OTFT mobility³¹. Without the addition of higher molecular weight polymer chains to act as tie chains, the frequency and prominence of the grain boundaries between crystalline regions force charges to move by unfavorable hopping events, severely limiting the charge carrier mobility²⁹. Based on OTFT studies, a decrease in the electronic mobility might be expected with lower molecular weight but studies using blended systems demonstrated that more favorable morphology can arise from an intermediate molecular weight³⁵. Although this has been shown for ladder-type polymers³⁶, conventional OECT materials, such as polythiophene or naphthalenediimide (NDI)-based polymers, have a less rigid structure. Thus, the link between molecular weight of ladder-type polymers and OECT performance cannot be translated directly to other OMIECs and the relationship between OECT performance and OMIEC molecular weight has not been decoupled yet.

Additionally, the purification of OMIEC polymers is rarely considered. The vast majority of OMIEC conjugated polymers are synthesized using Pd-mediated cross-coupling conditions^{19,24,25,28,37,38} and these materials are typically only purified by simple Soxhlet extraction in numerous solvents, which removes limited amounts of residual metal impurities. Specifically, Stille polymerizations make use of around 3000–5000 ppm of Pd, and while Soxhlet extraction can reduce levels by an order of magnitude, this may not be sufficient to maximize performance³⁹. These levels have been shown to impact OPV applications⁴⁰, as residual metals, such as palladium (Pd), may act as a charge sink, trapping mobile charges and reducing charge transport properties^{39,41}. Alternatively, Pd can act as a co-catalyst to facilitate charge transfer and catalyze redox reactions of ambient species (i.e., in the operation conditions used in OECT but not OTFT applications)⁴², including the oxygen reduction reaction (ORR), which generates toxic hydrogen peroxide, making impure OMIECs unsuitable for bioelectronic applications.

Herein, we present an investigation into the impact of purity (the level of residual Pd) and molecular weight of the most common p-type and n-type backbones (polythiophene and NDI, respectively, Fig. 1a) on the OECT performance. These were prepared by standard Stille polymerizations, using 2 mol% Pd catalyst (which equates to ~3000 ppm for p(g₄T2-TT) and ~4,900 ppm for p(C₆G₃NDI-T)), and the different molecular weights were obtained by preparative GPC (Fig. 1b, c), which conveniently offers the ability to narrow \mathcal{D} whilst simultaneously removing residual metal impurities. The optoelectronic properties, OECT performance, and structural properties using grazing incidence wide-angle X-ray scattering (GIWAXS) of four molecular weight fractions of $\mathcal{D} < 2$ (Table 1) of polymers p(g₄T2-TT) and p(C₆G₃NDI-T) were studied and compared to the unpurified polymer (i.e., the polymer after standard Soxhlet procedure but pre-fractionation). In particular, the impact of purity on the OECT performance was probed (Fig. 1).

This study utilizes an alternative method for OMIEC purification, by more thoroughly removing by-products than only using traditional Soxhlet purification. Preparative GPC is also particularly useful for studying the impact of molecular weight as any batch-to-batch variations are removed. One batch is simply divided into several fractions of lower dispersity instead of synthesizing new batches through different reaction conditions, making this the most comprehensive method for comparing molecular weights.

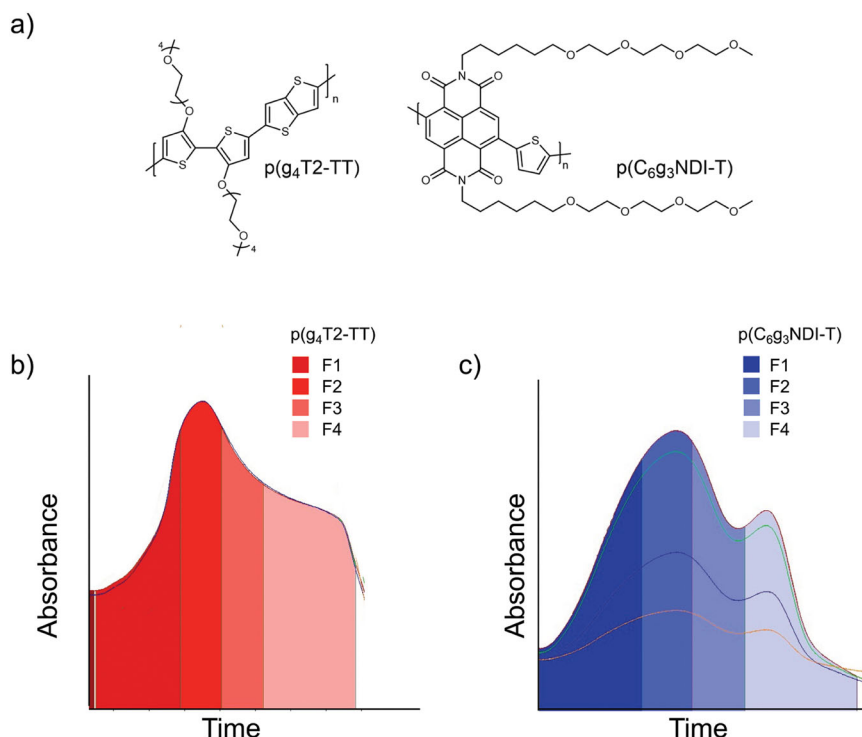


Fig. 1 | Chemical structures and fractionation traces of the two investigated polymer. **a** Chemical structures of $p(g_4T_2-TT)$ and $p(C_6g_3NDI-T)$. The preparative gel permeation chromatography trace for **b** $p(g_4T_2-TT)$ and **c** $p(C_6g_3NDI-T)$

showing the second cycle, where the polymer is collected into four separate fractions, F1–4.

Results and discussion

Material synthesis

The synthetic routes to $p(g_4T_2-TT)$ and $p(C_6g_3NDI-T)$ are shown in Supplementary Figs. 2–5. Monomer 13,13'-((5,5'-dibromo-[2,2'-bithiophene]-3,3'-diyl)bis(oxy))bis(2,5,8,11-tetraoxatridecane) ($g_4T_2Br_2$) was synthesized through a modified literature procedure, by utilizing a copper(I) iodide catalyst to decorate the 3,3'-dibromo-2,2'-bithiophene core with tetraethylene glycolated side chains, followed by a typical bromination using *N*-bromosuccinimide to generate the monomer in a 56% yield (Supplementary Fig. 6)⁴³. Alternatively, 4,9-dibromo-2,7-di(2,5,8,11-tetraoxaheptadecan-17-yl)benzo[*lmn*][3,8]phenanthroline-1,3,6,8(2*H*,7*H*)-tetraone ($C_6g_3NDI-Br_2$) was prepared from 2,6-dibromonaphthalene-1,4,5,8-tetracarboxylic dianhydride (NDA- Br_2) using a single step procedure, by treating NDA- Br_2 with 2,5,8,11-tetraoxaheptadecan-17-amine (Supplementary Fig. 7)²⁴. Lastly, both $p(g_4T_2-TT)$ and $p(C_6g_3NDI-T)$ were synthesized via Stille polymerization reactions of $g_4T_2Br_2$ or $C_6g_3NDI-Br_2$ respectively, with equimolar quantities of the appropriate stannylated thiophene derivative (Supplementary Figs. 8 and 9). Each polymer was initially purified using the traditional Soxhlet purification method. While this has been documented as a method for separating molecular weights⁴⁴, the disadvantage is that fractions eluting later will likely have a higher purity than those eluted first. Furthermore, none of these polymers were soluble in the Soxhlet solvents used prior to chloroform, so the dispersity could not be reduced by this method. Instead, we employed preparative GPC to separate a single batch of polymer into four molecular weight fractions, such that each fraction contained approximately the same amount of material, with the first fraction collected (fraction 1) being of highest molecular weight (Fig. 1b, c). Preparative GPC can also be viewed as an additional method of purification, as remaining impurities (typically Pd from the catalyst) are of different molecular weight than any polymer chains, thus are discarded before or after the elution of the polymer.

Materials' properties

Analytical GPC was employed to estimate the molecular weights of the two series of polymers and their weight fractions, with dimethylformamide and chloroform as eluent for $p(g_4T_2-TT)$ and $p(C_6g_3NDI-T)$, respectively. The measurements were conducted at 40 °C with respect to polystyrene standards. The values obtained are summarized in Table 1. It should be noted that despite glycolated polymers often

Table 1 | Summary of the two polymer series' physical and optoelectronic properties

Polymer		M_n (kDa) [\mathcal{D}] ^a	$E_{g,opt}$ (eV) ^b	$\lambda_{max, sol}$ (nm) ^c	EA (eV) ^d	IP (eV) ^d
$p(g_4T_2-TT)$	Unpurified	83.3 [1.36]	1.67	610	–	4.23
	F1	180.1 [1.30]			–	4.24
	F2	107.9 [1.12]			–	4.25
	F3	61.3 [1.25]			–	4.24
	F4	18.4 [1.15]			–	4.26
	Recombined	90.6 [1.28]				
$p(C_6g_3NDI-T)$	Unpurified	42.4 [2.13]	1.65	323, 540	4.19	–
	F1	211.0 [1.95]			4.18	–
	F2	99.8 [1.34]			4.18	–
	F3	46.2 [1.67]			4.17	–
	F4	17.6 [1.48]			4.19	–
	Recombined	61.2 [1.92]				

^aNumber-average molecular weight (M_n) and dispersity (\mathcal{D}) measured by GPC vs polystyrene standards in dimethylformamide for $p(g_4T_2-TT)$ or chloroform for $p(C_6g_3NDI-T)$ at 40 °C.

^bOptical band gap estimated from thin film UV-Vis absorption onset.

^cPeak wavelength obtained from solution UV-Vis absorption spectra in chloroform.

^dCalculated from the onset of the cyclic voltammogram of polymer thin films on glassy carbon electrode with 0.1M tetrabutylammonium hexafluorophosphate as the supporting electrolyte using a platinum counter electrode and a silver/silver chloride reference electrode (Supplementary Fig. 13).

Table 2 | Steady-state OECT performance of polymers

Polymer		Conc. of Pd [ppm] ^a	μ_{OECT} [$\text{cm}^2 \text{V}^{-1} \text{s}^{-1}$] ^b	C^* [F cm^{-3}] ^c	$[\mu C^*]$ [$\text{F V}^{-1} \text{cm}^{-1} \text{s}^{-1}$] ^d	g_m' [S cm^{-1}] ^e
p(g ₄ T2-TT)	Unpurified	1769	3.13 ± 0.52	120 ± 9	374 ± 67	295 ± 57
	F2	370	5.31 ± 2.65	246 ± 21	1308 ± 662	838 ± 438
	F1	323	5.65 ± 0.19	123 ± 15	694 ± 87	494 ± 17
	F3	157	6.53 ± 0.065	308 ± 20	2008 ± 130	1457 ± 6
	F4	73	8.53 ± 0.40	114 ± 14	972 ± 127	626 ± 38
	F3 + Pd ₂ (dba) ₃	2157	3.02 ± 0.26	287 ± 18	860 ± 56	602 ± 21
	Recombined ^f	236	4.75 ± 1.12	123 ± 17	451 ± 124	231 ± 56
p(C ₆ g ₃ NDI-T)	Unpurified	1176	1.02 × 10 ⁻³ ± 3.79 × 10 ⁻⁴	222 ± 79	0.227 ± 0.117	0.055 ± 0.021
	F4	540	2.26 × 10 ⁻³ ± 2.53 × 10 ⁻⁴	250 ± 78	0.563 ± 0.188	0.164 ± 0.018
	F1	197	3.57 × 10 ⁻³ ± 2.94 × 10 ⁻⁴	129 ± 55	0.461 ± 0.202	0.127 ± 0.017
	F3	112	6.06 × 10 ⁻⁴ ± 1.58 × 10 ⁻⁴	521 ± 160	0.316 ± 0.127	0.095 ± 0.024
	F2	39	5.34 × 10 ⁻³ ± 3.40 × 10 ⁻⁴	306 ± 127	1.632 ± 0.688	0.155 ± 0.020
	F2 + Pd ₂ (dba) ₃	2039	1.10 × 10 ⁻³ ± 1.52 × 10 ⁻⁴	124 ± 26	0.136 ± 0.0341	0.029 ± 0.003
	Recombined ^f	198	1.96 × 10 ⁻³ ± 2.25 × 10 ⁻⁴	257 ± 101	0.503 ± 0.205	0.110 ± 0.012

^aCalculated from inductively coupled plasma mass spectrometry (ICP-MS, detailed in the SI).

^bOECT mobility calculated from the transistor saturation μC^* product using the respective C^* values.

^c C^* values extracted from Randles circuit fits from electrochemical impedance curves of the polymers coated on Au electrodes in 0.1 M aqueous NaCl solution.

^d $[\mu C^*]$ calculated for the highest performing channel from the slope of g_m with known channel dimensions and applied bias.

^ePeak OECT transconductance normalized by thickness.

^fFormed by combining a mass ratio of 1:1.32:0.16:1 of F1:F2:F3:F4 for p(g₄T2-TT), which resulted in M_n = 90.6 kDa and a mass ratio of 1:1.4:1.4:1 of F1:F2:F3:F4 for p(C₆g₃NDI-T), which resulted in M_n = 61.2 kDa. All measurements are an average across 6 devices.

exhibiting a bimodal distribution from GPC^{19,25}, these polymers, particularly once fractionated, showed ideal unimodal traces (Supplementary Figs. 10–12). This is expected, as the preparative GPC used for fractionation relies upon the same size exclusion method as the analytical GPC.

The two series' optoelectronic properties are summarized in Table 1. Cyclic voltammetry (CV) in 0.1 M tetrabutylammonium hexafluorophosphate (TBAPF₆) in acetonitrile was used to determine the ionization potential (IP) of p(g₄T2-TT), which remained unchanged across the fractions at -4.25 eV, providing an estimate for the highest occupied molecular orbital (HOMO) (Supplementary Fig. 13a)⁴⁵. The electron affinity (EA) of p(C₆g₃NDI-T) also showed no significant variation at -4.18 eV and provided an estimate for the lowest unoccupied molecular orbital (LUMO) (Supplementary Fig. 13b). Each polymer exhibited partly reversible discrete reduction or oxidation behavior. Due to the relatively narrow electrochemical stability window of the electrolyte, the EA for p(g₄T2-TT) and IP for p(C₆g₃NDI-T) could not be accessed using this method.

The UV-Vis absorption spectra of the polymers in solution and as thin films are presented in Supplementary Figs. 14 and 15, respectively. p(g₄T2-TT) showed a characteristic absorption profile as seen in previous reports of similar polymers⁴⁶, where the λ_{max} (≈600 nm) is attributed to the π - π^* transition (HOMO-LUMO transition), while the small lower energy band (≈950 nm) is most likely attributed to ambient-induced polarons. As observed previously, both bands for p(C₆g₃NDI-T) were blue-shifted to higher energy compared to p(g₄T2-TT), with the π - π^* transition ≈345 nm and the peak ≈600 nm attributed to the intramolecular charge transfer (ICT) from the electron-rich bithiophene units to the electron-deficient NDI units^{24,47,48}. In the UV-Vis absorbance spectra in solution of p(g₄T2-TT) (Supplementary Fig. 14a), no band at ≈950 nm is observed, confirming its attribution to doping by ambient species in the solid-state. The normalized UV-Vis data supported the uniformity noted by CV for each polymer series, providing almost identical spectra across the molecular weights, which is unsurprising, given that no impact on the bandgap is expected above the effective conjugation limit. The subtle differences observed in the vibronic structure for p(g₄T2-TT) and the shift of the ICT band for p(C₆g₃NDI-T) indicated that different packing may be induced by

the change in molecular weight (more clearly indicated in Supplementary Information, Supplementary Fig. 16).

Inductively coupled plasma mass spectrometry (ICP-MS) was employed to calculate the concentration of residual palladium contaminants in each fraction (Table 2), which originates from the Pd-based catalysts required for Stille polymerizations. In both polymers, the levels of palladium observed before preparative GPC fractionation were on the same order of magnitude, at 1769 and 1176 ppm, for the p-type and n-type polymers, respectively. For both OMEC polymers, this data demonstrated the impact of preparative GPC fractionation on purity, whereby all fractions contained less Pd than the unpurified fractions, with a decrease of between 54 and 97% in Pd levels observed. This translated to Pd levels as low as 39 and 73 ppm, validating preparative GPC as a consistent method for purification.

To investigate the impact of fractionation (reduced dispersity and reduced concentration of Pd) on the polymer microstructure, grazing incidence wide-angle X-ray scattering (GIWAXS) measurements were carried out. The line-cuts of the as-spun thin films are displayed in Fig. 2 and the 2D GIWAXS patterns and peak parameters are included in the Supplementary Information (Supplementary Figs. 17 and 18). p(g₄T2-TT) compared well to previously reported glycolated polythiophene derivatives^{28,43}, presenting an edge-on orientation. To quantitatively interpret the GIWAXS data, pseudo-Voigt peak fits were used to extract disorder associated coherence lengths in the backbone and lamellar directions. The unpurified p-type polymer had a poorly resolved π -stack compared to the four fractions, which may be because of the larger δ (Table 1). Notably, after fractionation, the in-plane π -stack contracted by 0.05–0.09 Å and displayed longer coherence lengths (narrower diffraction peaks) in the backbone direction compared to the unpurified polymer (Supplementary Fig. 17). p(g₄T2-TT) showed evidence of two orders of out-of-plane lamellar scattering, with the fractions showing expanded lamellar spacing and a reduction in the coherence length in the lamellar direction of 10–25%.

Contrastingly, p(C₆g₃NDI-T) showed a face-on orientation, in agreement with previously reported NDI polymers^{19,49}. The (010) out-of-plane π -stack scattering displayed broad and relatively weak peaks due to scattering arising from a small number of chains stacked together, which can usually be attributed to a high degree of

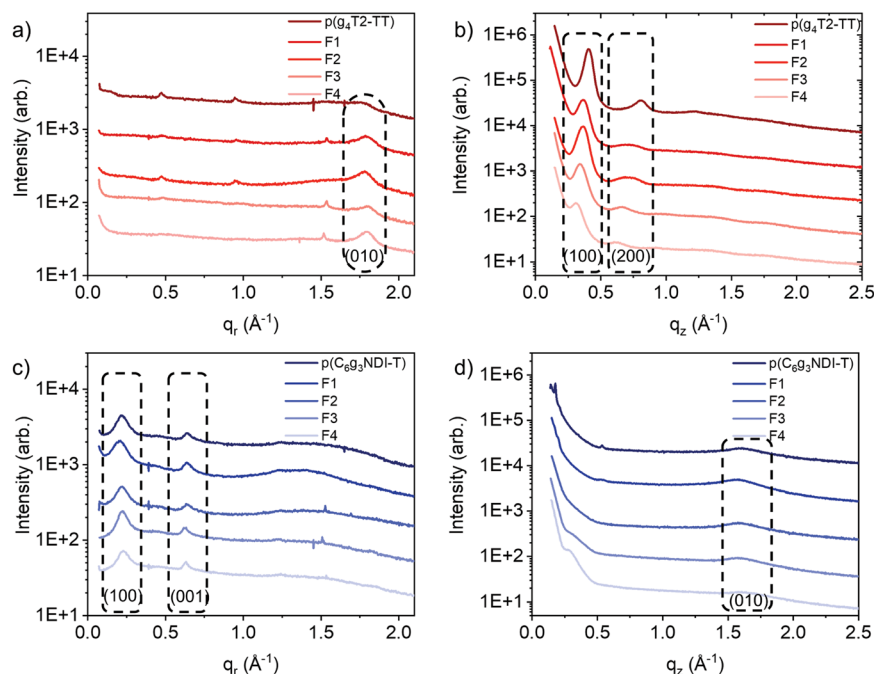


Fig. 2 | Two-dimensional grazing incidence wide angle X-ray scattering. GIWAXS line cuts of as-cast thin films of the unpurified and four fractions of the two polymers, showing **a** in-plane (q_r) and **b** out-of-plane (q_z) line cuts of each fraction of

$p(g_4T_2-TT)$ and **c** in-plane and **d** out-of-plane line cuts of each fraction of $p(C_6g_3NDI-T)$.

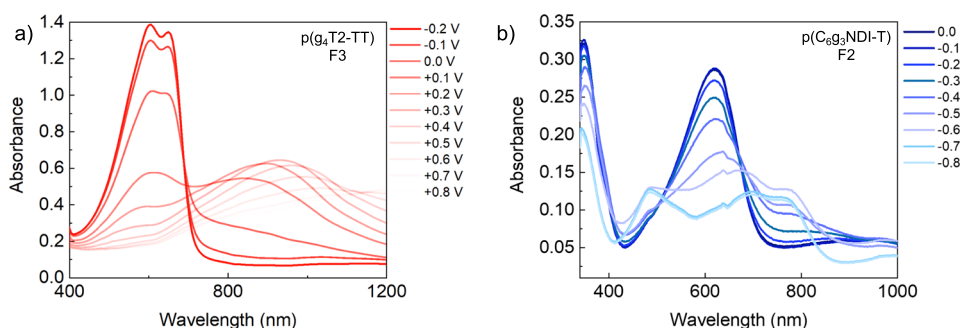


Fig. 3 | Spectroelectrochemical measurements for the highest performing fraction of each polymer. UV-Vis absorption measurements recorded whilst applying a voltage vs Ag/AgCl using a 0.1 M NaCl aqueous degassed electrolyte,

with potential steps of 0.1 V. **a** Fraction 3 of $p(g_4T_2-TT)$ between -0.2 and $+0.8$ V vs Ag/AgCl and **b** fraction 2 of $p(C_6g_3NDI-T)$ between 0.0 and -0.8 V. The unpurified and other fractions for each polymer are shown in Supplementary Fig. 20.

paracrystalline disorder⁵⁰. A trend in π - π stacking distance was observed, with a small expansion in the out-of-plane d -spacing with increasing M_n . This also corresponds to the bathochromic shift observed in the ICT band in the UV-Vis absorption spectra with decreasing molecular weight, indicating subtle differences in packing (Supplementary Fig. 16b). Previous results have shown that for NDI-T2 backbones, two different packing configurations are possible, namely Form I and Form II⁵¹. Form I occurs where the NDI motif aligns with an NDI from a neighboring chain through cofacial registration, resulting in double the backbone periodicity, whilst in a Form II configuration the NDI unit aligns with a bithiophene unit⁵¹. For $p(C_6g_3NDI-T)$, the (001) in-plane backbone spacing of 19.6 – 20.0 Å was consistent with the length of an NDI-T repeat length, thus it can be assumed that predominantly Form I stacking was present.

The electrochemical activity of both series of polymers was further investigated in 0.1 M NaCl aqueous electrolyte through CV and spectroelectrochemical measurements. Aqueous CV (Supplementary Fig. 19) indicated that both polymers at all molecular weights were reversibly doped and de-doped. All fractions of $p(g_4T_2-TT)$ showed comparable oxidation onset potentials of ≈ -0.1 V versus Ag/AgCl. The

same is true for $p(C_6g_3NDI-T)$, where similar reduction onsets of ≈ -0.1 V versus Ag/AgCl were recorded. Their doping mechanisms were further explored by spectroelectrochemical measurements, conducted in the same electrolyte. As shown in Fig. 3, Fig. 2a and Supplementary Figs. 20a and 21a, all fractions of $p(g_4T_2-TT)$ were partially doped under ambient conditions and require a negative potential to fully de-dope the films, as indicated by the negative oxidation onset potential. Progressive charging to $+0.2$ V versus Ag/AgCl showed a gradual bleaching of the π - π^* peak, with a simultaneous appearance of a new absorption peak at ≈ 950 nm, which was attributed to the formation of the polymer's polaron, as described in previous literature^{28,52}. Beyond $+0.3$ V, this peak began to decrease in intensity and a new peak at higher wavelengths appeared, which is ascribed to the formation of bipolaronic species. Finally, the applied voltage was returned to the initial value of -0.2 V and all fractions of the polymer resumed their original de-doped UV-Vis absorption spectra, indicating good reversibility, with no polymer degradation, in aqueous media.

The n-type polymer, $p(C_6g_3NDI-T)$, was charged between 0.0 and -0.8 V versus Ag/AgCl (Fig. 3, Fig. 2b, and Supplementary Figs. 20b and 21b), and all fractions showed a fully de-doped state at 0 V. Generally,

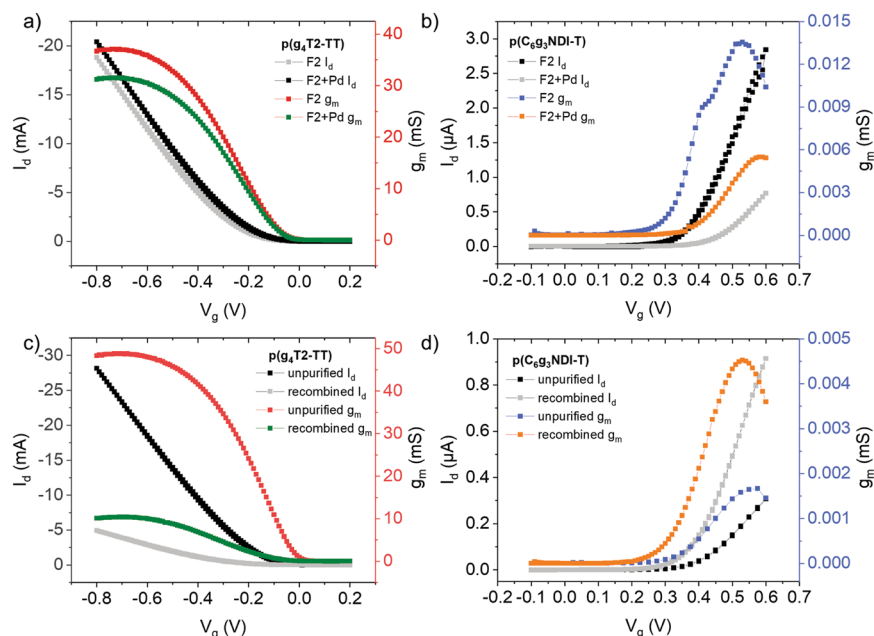


Fig. 4 | OECT transfer and transconductance characteristics before and after the reintroduction of Pd and comparing the unpurified and recombined batches of each polymer. The OECT transfer and transconductance characteristics for **a** fraction 3 of p(g₄T2-TT) before and after the reintroduction of 2000 ppm of Pd and **b** fraction 2 of p(C₆g₃NDI-T) before and after the reintroduction of 2000 ppm

of Pd. Transfer and transconductance characteristics for **c** unpurified and recombined p(g₄T2-TT) and **d** unpurified and recombined p(C₆g₃NDI-T). All measurements are an average across 6 devices. I_d refers to the drain current, V_g is the gate voltage and g_m is the transconductance.

by charging at -0.8 V, the ICT band intensity decreases, while two new absorption features appear at ≈ 480 nm and ≈ 790 nm. They are assigned to transitions to the S1 and S2 states, which are dominated by π - π^* and ICT, as suggested by literature⁴⁷. Notably, all fractions displayed a large doping extent, which was reversible, as shown by a return to the fully de-doped polymer UV-Vis absorption spectrum when charging is returned to the initial value. From the consistent UV, CV and spectroelectrochemical data across all fractions of the two polymers, it was concluded that the degree of doping remains constant, and not dependent on the molecular weight or the degree of purity in both cases.

Organic electrochemical transistor performance

OECT devices were fabricated and the electrical performance measured for each fraction, in order to elucidate the impact of the palladium. The devices were fabricated according to the procedure described in the Methods section, with a device geometry of $W = 100$ μ m and $L = 10$ μ m. All devices were operated in accumulation mode, and data was obtained without any post-processing treatments (see Supplementary Figs. 22–25 for output, transfer and transconductance curves) and Table 2 summarizes the OECT parameters.

The impact of Pd impurities on the OECT performance was firstly evaluated by comparing the Pd concentrations in each fraction, measured by ICP-MS, to the charge carrier mobilities (Table 2). Across F1–4 of both materials, where Pd concentrations are reduced, the charge carrier mobility is increased in seven out of eight cases (Table 2). We propose that the origins of these observations arise from the Pd(0) nanoclusters, formed from the molecular Pd cross-coupling catalyst during the polymerization reactions^{40,53,54}. Such species may be able to act as catalysts for ORR due to the favorable energetic offsets⁵⁵. For example, the LUMO of p(C₆g₃NDI-T) has an energy of approximately -4.18 eV, considerably higher than the -5.1 to -5.2 eV work function of Pd^{56,57}, meaning that both the electron transfer from the polymer electron polaron to Pd and the ORR itself are energetically favorable, leading to polaron annihilation. This mechanism of charge transfer explains why the n-type polymer

observes a significant increase in mobility upon the removal of Pd. When mobile electrons are transferred to the Pd(0) nanoclusters to catalyze the ORR, the electron mobility is reduced. It should be noted that this reaction is only possible in aqueous conditions, such as those used in OECT operation. Additionally, ORR can also generate hydrogen peroxide, which is biologically toxic, hindering any application as a safe bioelectronic sensor⁵⁸. Interestingly the mobility of the p-type material was observed to be negatively affected by higher palladium levels, albeit by a smaller factor than the n-type (twofold decrease compared to fivefold). There are no accessible oxidation reactions in this case that could be driven by the hole polaron energies. **Impedance measurements on p-type polymers with similar energy levels to p(g₄T2-TT) have previously indicated that increased Pd content can cause increased electrical resistance⁴¹. It is possible that the presence of Pd nanoclusters in the OECT polymer thin films creates local distortions in the semiconductor microstructure, and a subsequent increase in energetic disorder, leading to a reduction in mobility observed^{40,41,59}.**

In addition to containing differing concentrations of palladium, each sample however also differed in both molecular weight and dispersity. To decouple the influence of these parameters on the OECT charge carrier mobilities, all GPC fractions for each polymer were recombined and the OECT characteristics were measured (see recombined rows in Table 2, Fig. 4c, d, and Supplementary Figs. 26 and 27). In this way, any effects arising from the molecular weight variations or reduced dispersities of the fractionated batches are eliminated. Furthermore, the physical form of Pd is representative of that present in the unpurified polymers (i.e., nanoclusters vs molecular Pd). The impact of purification appears to offer a greater improvement for p(C₆g₃NDI-T) than p(g₄T2-TT). More specifically, there is a 92% increase in electron mobility from 1.02×10^{-3} to 1.96×10^{-3} $\text{cm}^2 \text{V}^{-1} \text{s}^{-1}$ for p(C₆g₃NDI-T), compared to $\sim 50\%$ increase in hole mobility for p(g₄T2-TT), from 3.13 to 4.75 $\text{cm}^2 \text{V}^{-1} \text{s}^{-1}$, where both have comparable levels of Pd, at around 200 ppm. The recombined batches of both polymers show comparable C^* values to the unpurified batches, resulting in increases to μC^* from 0.227 to 0.503 $\text{FV}^{-1} \text{cm}^{-1} \text{s}^{-1}$ for

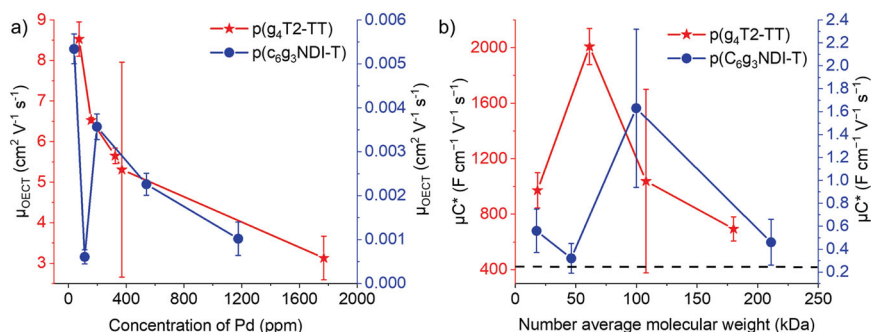


Fig. 5 | Comparing concentration of Pd and the molecular weight with the OECT performance. **a** μ_{OECT} as a function of Pd content in ppm for $p(\text{g}_4\text{T}_2\text{-TT})$ and $p(\text{C}_{6g_3}\text{NDI-T})$ and **b** $[\mu\text{C}^*]$ as a function of M_n for $p(\text{g}_4\text{T}_2\text{-TT})$ and $p(\text{C}_{6g_3}\text{NDI-T})$,

whereby the dashed line indicates the performance of the polymer pre-fractionation. The error bars are the standard deviation of the data set and μ_{OECT} is the calculated OECT mobility.

$p(\text{C}_{6g_3}\text{NDI-T})$ and from 374 to $451 \text{ F cm}^{-3} \text{ V}^{-1} \text{ s}^{-1}$ for $p(\text{g}_4\text{T}_2\text{-TT})$. Notably the recombined batches of both polymers show a lower performance than most of the fractions. This can be explained by the GIWAXS data (Fig. 2 and Supplementary Figs. 17 and 18), where fractionation resulted in both a decrease in π - π stacking distance and an increase in coherence length, both of which would be expected to result in an increase in charge carrier mobility.

To further explore the causal relationship between the concentration of Pd and the OECT performance, we reintroduced 2000 ppm of Pd back into the highest performing fraction, in the form of the $\text{Pd}_2(\text{dba})_3$ catalyst. The OECT characteristics were remeasured (Fig. 4a, b). For fraction 3 of $p(\text{g}_4\text{T}_2\text{-TT})$, this resulted in lower performance, with hole mobility decreasing from 6.53 to $3.02 \text{ cm}^2 \text{ V}^{-1} \text{ s}^{-1}$ (Fig. 4a and Supplementary Fig. 28). For fraction 2 of $p(\text{C}_{6g_3}\text{NDI-T})$, the reintroduction of Pd also resulted in the mobility decreasing from 5.34×10^{-3} to $1.10 \times 10^{-3} \text{ cm}^2 \text{ V}^{-1} \text{ s}^{-1}$ (Fig. 4b and Supplementary Fig. 29). The p-type polymer observed a smaller decrease than the n-type polymer, which is consistent with the relative differences observed between the unpurified and remixed sample measurements.

Ionic impurities in thienothiophene-based polymers have previously been shown to also have little impact on charge carrier mobility in OFET devices⁶⁰. To explore this correlation in our polymers, the unpurified and highest OECT performance fraction of each polymer were tested in a top gate/bottom contact OTFT and compared, (the output and transfer characteristics for which can be found in Supplementary Figs. 30 and 31). The n-type polymer, $p(\text{C}_{6g_3}\text{NDI-T})$, displayed low output currents, which resulted in poor electron mobilities of 1.7×10^{-4} and $6.0 \times 10^{-5} \text{ cm}^2 \text{ V}^{-1} \text{ s}^{-1}$ for the unpurified and fraction 2, respectively. Interestingly, the unpurified batch exhibits an order of magnitude greater electron mobility than the fractionated batch, supporting previous observations that material purity has little impact on OTFT performance. Instead, it is possible that the higher molecular weights present in the unpurified batch led to more favorable morphology, which is a dominant effect for OTFT performance. The hole transporting polymer, $p(\text{g}_4\text{T}_2\text{-TT})$, displayed conducting properties with no current modulation, so no mobility was able to be extracted.

For the $p(\text{g}_4\text{T}_2\text{-TT})$ series, the thickness normalized transconductance increased to a peak of 1457 S cm^{-1} for fraction 3 (concentration of Pd = 157 ppm), then decreased as the M_n further increases. A similar trend is observed for $p(\text{C}_{6g_3}\text{NDI-T})$, where the highest normalized transconductance was observed for fraction 2 (concentration of Pd = 39 ppm), at 0.155 S cm^{-1} . Interestingly, for both series, all values of the fractions were larger than that of the unfractionated batch, which is likely to be caused by the increased charge carrier mobility. $[\mu\text{C}^*]$ was calculated using Eq. (1), where the same trends were observed, with the p-type increasing from 694 to 1308 to $2008 \text{ F cm}^{-3} \text{ V}^{-1} \text{ s}^{-1}$, a very high OECT performance^{23,28,61,62}, then decreasing to $972 \text{ F cm}^{-3} \text{ V}^{-1} \text{ s}^{-1}$ (Fig. 5a). $p(\text{C}_{6g_3}\text{NDI-T})$ also

mimicked the thickness normalized transconductance, with fraction 2 (the lowest concentration of Pd, at 39 ppm) providing the maximal $[\mu\text{C}^*]$ value at a polymer-best $1.632 \text{ F cm}^{-3} \text{ V}^{-1} \text{ s}^{-1}$ (Fig. 5b).

These trends were further probed by performing electrochemical impedance spectroscopy (EIS) to determine the volumetric capacitance at offset potentials of 0 to -0.8 V and 0.3 to 0.8 V against Ag/AgCl, for p- and n-type devices, respectively, with a $0.1 \text{ M NaCl}_{(\text{aq})}$ electrolyte (see Supplementary Figs. 32 and 33). For $p(\text{g}_4\text{T}_2\text{-TT})$, C^* increased from 114 F cm^{-3} to reach a peak for fraction 3 of 308 F cm^{-3} , before decreasing by $\sim 60\%$. A similar observation was made for $p(\text{C}_{6g_3}\text{T}_2\text{-T})$, where again fraction 3 provides the optimal C^* of 521 F cm^{-3} . Both trends were supported by the doping efficiency seen by spectroelectrochemical measurements, whereby the π - π^* transition in each case was normalized to one and the peak associated with the polaron was plotted against each voltage (Supplementary Fig. 21).

It is expected that this trend is observed due to the microstructure of fraction 3 providing the optimal arrangement to promote ionic miscibility³. As it is known that the microstructure is influenced by the molecular weight^{31,33}, and it is therefore suggested that the molecular weight of fraction 3 is optimal for a high C^* value. As documented in literature, a high C^* value may indicate that whilst a polymer is able to accommodate compensatory ions, this results in a disruption to the microstructure, leading to a decreased mobility^{28,63}. This can be partially observed for both polymer series, for example, fraction 3 of $p(\text{C}_{6g_3}\text{NDI-T})$ had the highest C^* value, but the lowest μ_{OECT} despite lower concentration of electron trapping Pd. This demonstrates that a fine balance between μ_{OECT} and C^* is required to maximize OMIEC performance in OECTs, which can evidently be influenced by polymer molecular weight. Whilst molecular weight may to some extent impact OECT performance (evaluated by g_m and $[\mu\text{C}^*]$), both polymer series indicate that the palladium concentration has more influence.

Another critical aspect of OECT performance is the operational stability of devices. Device stability was measured by cycling the gate potential and recording the drain current over 30 min. Generally, it was observed that the stability of the polymer was improved when the Pd content was reduced, with the fractionated materials exhibiting better stability than the unpurified batches (Supplementary Figs. 34 and 35). Numerically, this translates to a change in drain current of 7% for one of the purified fractions of $p(\text{C}_{6g_3}\text{NDI-T})$, compared to a 36% change for the unpurified batch (Fig. 6). Similarly, the stability of the p-type polymer improved from a 66% change in drain current for the unpurified batch, to a change of 28% for fraction 2 (Fig. 6). This generates hydrogen peroxide in a two-electron process, which is likely detrimental to OECT performance and can cause degradation of both the OMIEC and the electrodes^{38,64}. This therefore indicates that the purity of the polymer plays a role in determining both OECT performance and stability.

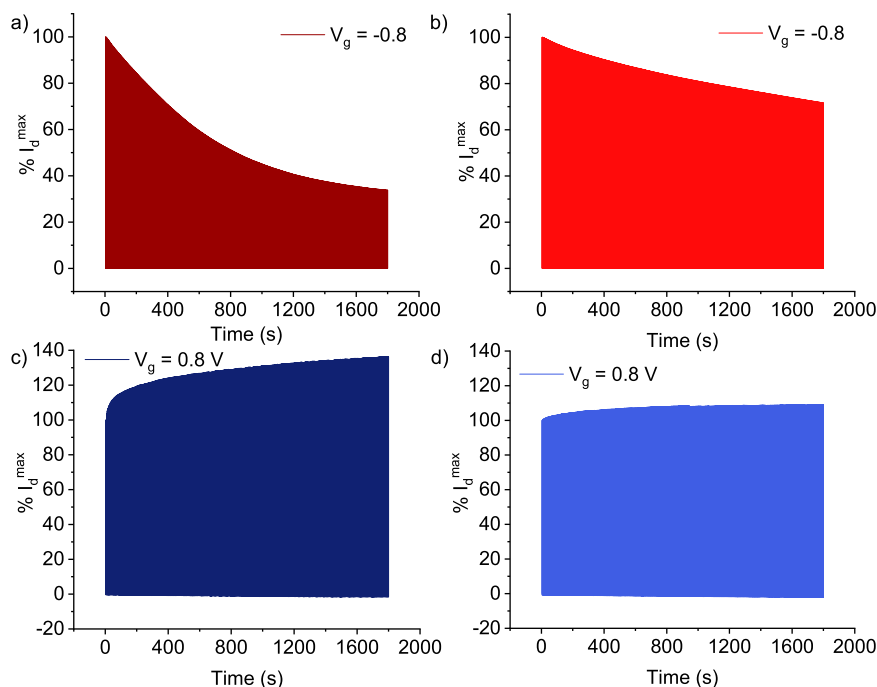


Fig. 6 | OECT stability measurements in 0.1 M NaCl aqueous electrolyte. Probing stability by cycling V_g and recording I_d over 30 min. The graphs indicate the percentage decrease in drain current (I_d) for **a** unpurified $p(g_4T_2-TT)$, **b** F2 of $p(g_4T_2-TT)$, **c** unpurified $p(C_6g_3NDI-T)$, and **d** F2 of $p(C_6g_3NDI-T)$.

To summarize, this study explores the influence of polymer purity and molecular weight on the two most common polymer backbones for OECT applications, a p-type polythiophene and an n-type NDI material. These materials employed preparative GPC as a purification technique for polymers, fractionating a single polymer batch into four batches. By studying the optoelectronic properties using UV-Vis absorption, CV and spectroelectrochemical measurements, the structural properties using GIWAXS and the OECT characteristics, the impact of OMIEC purity on the OECT performance of polymers $p(g_4T_2-TT)$ and $p(C_6g_3NDI-T)$ was examined.

To better understand the trend in performance observed across a range of palladium concentrations, particularly the charge carrier mobility, OECT devices were fabricated and measured. We found that the reduced palladium significantly improved the OECT performance, arising mainly from an increase in mobility (of ~60% and 80% for the p- and n-type, respectively), when comparing the unpurified fractions with the purified fractions. We hypothesize that residual Pd arranges in nanoclusters, which act to trap charges and as a co-catalyst for ORR, reducing OMIEC stability. These findings were further verified by reintroducing 2,000 ppm of Pd into the highest performing fraction of each polymer, which saw significant decreases in the OECT mobilities.

These observations highlight the importance of synthetic purification of any semiconducting polymer to be employed in an ambient, aqueous environment. For a valid comparison between OMIECs and to derive accurate structure-property relationships, this work indicates that Pd levels must be as low as possible. As this observation applies to both p- and n-type materials, proper purification of new and existing OMIECs will enhance understanding of OMIECs and improve OECT performance, and preparative GPC offers a versatile method to achieve this.

Methods

Materials' characterization

Column chromatography was performed on silica gel from VWR Scientific, using the indicated solvents. Thin layer chromatography was performed on Silicagel 60 F254 plates purchased from Merck. 1H and ^{13}C NMR spectra were recorded on a Bruker AV-400 spectrometer at

298 K, with chemical shifts (δ) are expressed in parts per million (ppm) downfield from tetramethylsilane (TMS). Deuterated solvents were purchased from Sigma Aldrich. Electrospray (ES-ToF) mass spectrometry was performed using a Micromass LCT Premier. Recycling preparative HPLC was performed using a LaboACE LC-5060 instrument with a separation line containing a 4HH column. The polymers were injected as 5 mg mL⁻¹ solutions in chloroform and collected at intervals such that each fraction was approximately one quarter of the material injected, then the solvent removed in vacuo. For OECT characteristics where palladium was reintroduced to the best performing fractions, 2,000 ppm of Pd₂(dba)₃ was dissolved in 5 mg mL⁻¹ solution of the polymer in chloroform. For OECT characteristics where fractions 1–4 were recombined, this was done so in a mass ratio of 1:1.4:1.4:1 for F1:F2:F3:F4 in order to replicate the original molecular weight profile, and solutions of 5 mg mL⁻¹ were used for spin coating the devices. For measurements requiring thin films (UV-vis absorption, spectroelectrochemical measurements, grazing incidence wide-angle X-ray scattering, electrochemical impedance spectroscopy and transistor properties), these were formed by spin coating 50 μ L of 5 mg mL⁻¹ polymer solutions onto cleaned glass, silicon wafers, ITO or transistor substrates and allowed to air dry. Grazing incidence wide-angle X-ray scattering (GIWAXS) was conducted at the Advanced Photon Source (APS) at Argonne National Laboratory using an incident beam energy of 10.92 keV and an incident angle of 0.14°. Raw scattering data were processed using GIXSGUI⁶⁵ and analyzed using a custom MATLAB script. For inductively coupled plasma mass spectrometry (ICP-MS) measurements, element concentrations were determined based on dry polymer weight. Samples were digested in TraceMetal® grade concentrated nitric acid under elevated temperature (200 °C) and pressure in fluoropolymer pressure vessels in a CEM MARS5 microwave digestion system. Digested samples were diluted with 2% v/v nitric acid prior to analysis to target an estimated 1–100 μ g/L in the analytical solution. Analysis was performed on an Agilent 8900 ICP-MS attached to an Agilent SPS-4 autosampler. The sample introduction system also includes a standard Scott double pass cooled spray chamber operated at 2 °C, a 2.5 mm i.d. Agilent glass torch, and a 200 μ L/min Micromist nebulizer. The ICP-MS was fitted with standard

nickel cones and operated in no gas mode. Before analysis, all solutions were further diluted by 50% by teeing in an internal standard solution of 2 µg/L platinum and rhodium (High Purity Standards) prepared with 2% v/v nitric acid to correct for instrumental drift. Procedural blanks were run in parallel with samples and averaged 14 ng contributing to less than 2% of the analytical signal and are regarded as negligible. Reproducibility is estimated to be 2.8% RSD from repeated analyses ($n = 11$) over 2 analytical sessions of an in-house QC sample prepared from a polymer of known Pd composition.

Electrochemical characterization

UV-Vis absorption spectra were recorded on UV-1601 (λ_{max} 1100 nm) UV-VIS Shimadzu UV-Vis spectrometers. Solution UV-Vis absorption spectroscopy was conducted on chloroform solutions with a polymer concentration of 0.006 mg mL⁻¹. UV-Vis absorption spectra were also recorded for thin films of the polymers on glass substrates. Cyclic voltammetry was performed employing an Autolab PGSTAT101 with a standard three-electrode configuration, including polymer-coated glassy carbon rod as the working electrode, a platinum wire as the counter electrode and an Ag/AgCl wire electrode as the reference electrode. The polymer was drop cast onto the glassy carbon electrode from 5 mg mL⁻¹ solutions and allowed to air dry before each measurement. The supporting electrolyte employed was a 0.1 M tetrabutylammonium hexafluorophosphate in acetonitrile solution or 0.1 M aqueous NaCl solution and was degassed for 30 min before use. The scan rate was 0.1 V s⁻¹ and the second and third scans are displayed in each figure herein. Spectroelectrochemical measurements were obtained from thin films of the polymer on ITO glass slides with the corresponding semiconductor. This was then connected in the same three-electrode configuration as for the cyclic voltammetry experiment and placed within a cuvette holder. The resulting electrochemical setup was then configured to reside inside the UV-1800 Shimadzu UV-Vis spectrometer previously employed for determining the optical properties of the polymers.

Transistor fabrication and characterization

OECT substrates were fabricated following previously reported photolithographic techniques⁴⁶. The OECT devices featured gold contacts making up a channel with width = 100 µm and length = 10 µm. To mitigate the problems with the parylene lift-off with p-type polymers, the substrates underwent a pre-deposition surface treatment to promote adhesion of the polymer film to the channels and electrodes⁶⁶. The polymer solutions (5 mg mL⁻¹) were deposited by spin-coating at 1000 rpm and 500 rpm for the p- and n-type polymers, respectively, for 45 s before air drying and peeling off the sacrificial parylene layer. Transistor properties were measured using an aqueous 0.1 M NaCl solution as the supporting electrolyte and an Ag/AgCl pellet electrode as the gate electrode and presented data is an average across 6 devices. Output and transfer characteristics, as well as stability measurements were recorded by connecting OECTs to an IviumStat potentiostat. Data was recorded through custom built LabVIEW software. Electrochemical impedance spectroscopy was performed using the same potentiostat, employing 600 µm × 600 µm polymer coated gold electrodes as the working electrode, with an Ag/AgCl pellet electrode as the gate electrode. For electrochemical impedance spectroscopy experiments a frequency range between 100 kHz to 1 Hz and an AC amplitude of 10 mV over a DC voltage above the threshold for the polymer. All OFET films were prepared and characterized under a nitrogen atmosphere. Borosilicate substrates were cleaned by sequential ultrasonication in a dilute Extran 300 detergent solution and deionized water for 30 min each. Then the substrates were cleaned with acetone and isopropyl alcohol by ultrasonication for 10 min each. As source-drain electrodes, 35 nm of Au with 5 nm of Al as the sticking layer was thermally evaporated at 2 × 10⁻⁶ mbar. The substrates with patterned Au/Al source-drain contacts were subjected to a UV-ozone treatment step

for 20 min. The channel width and length of the transistors were 1000 µm/40 µm. Before the film deposition, the polymers were dissolved in anhydrous chloroform. The solutions were kept under stirring on a hot plate at room temperature for overnight. As gate dielectric, the mixture of Cytop (CTL-809M) and its solvent (CT-SOLV 180) with a volume ratio of 2:1 was spin-coated at 1200 rpm for 60 s. The Cytop film was then thermally annealed at 50 °C for 2 h before the deposition of Al as a gate electrode. The electrical characteristics of the OTFTs were monitored by a probe station placed in an N₂-filled glove box that is connected to an Agilent B1500A semiconductor parameter analyzer. The saturation-regime mobility (μ_{sat}) of the transistor was determined using the equation $\mu_{\text{sat}} = 2L/WC_i \left(\frac{dI_d}{dV_g} \right)^{1/2}$, where I_d is the source-drain current, C_i is the capacitance per unit area, L is the channel length, W is the channel width, and V_g is the gate voltage.

Data availability

The authors declare that the data supporting the findings of this study are available within the paper and its Supplementary Information files. Additional data are available from the corresponding author upon request. The data acquired at the University of Bern that support the results of this study are available as open access in BORIS at <https://doi.org/10.48620/183>.

References

- Paulsen, B. D., Tybrandt, K., Stavrinidou, E. & Rivnay, J. Organic mixed ionic–electronic conductors. *Nat. Mater.* **19**, 13–26 (2020).
- Chen, H. et al. Acene ring size optimization in fused lactam polymers enabling high n-type organic thermoelectric performance. *J. Am. Chem. Soc.* **143**, 260–268 (2021).
- Marks, A. et al. Synthetic nuances to maximize n-type organic electrochemical transistor and thermoelectric performance in fused lactam polymers. *J. Am. Chem. Soc.* **144**, 4642–4656 (2022).
- Melling, D., Martinez, J. G. & Jager, E. W. H. Conjugated polymer actuators and devices: progress and opportunities. *Adv. Mater.* **31**, 1808210 (2019).
- Li, K. et al. Lattice-contraction triggered synchronous electrochromic actuator. *Nat. Commun.* **9**, 4798 (2018).
- Rashid, R. B. et al. Ambipolar inverters based on cofacial vertical organic electrochemical transistor pairs for biosignal amplification. *Sci. Adv.* **7**, eabh1055 (2021).
- Guo, K. et al. Rapid single-molecule detection of COVID-19 and MERS antigens via nanobody-functionalized organic electrochemical transistors. *Nat. Biomed. Eng.* **5**, 666–677 (2021).
- Romele, P. et al. Multiscale real time and high sensitivity ion detection with complementary organic electrochemical transistors amplifier. *Nat. Commun.* **11**, 3743 (2020).
- Marks, A., Griggs, S., Gasparini, N. & Moser, M. Organic electrochemical transistors: an emerging technology for biosensing. *Adv. Mater. Interfaces* **9**, 2102039 (2022).
- Lundberg, P. et al. Thermally activated delayed fluorescence with 7% external quantum efficiency from a light-emitting electrochemical cell. *Nat. Commun.* **10**, 5307 (2019).
- Tang, S. et al. Design rules for light-emitting electrochemical cells delivering bright luminance at 27.5 percent external quantum efficiency. *Nat. Commun.* **8**, 1190 (2017).
- Tan, S. T. M. et al. Redox-active polymers designed for the circular economy of energy storage devices. *ACS Energy Lett.* **6**, 3450–3457 (2021).
- Moia, D. et al. Design and evaluation of conjugated polymers with polar side chains as electrode materials for electrochemical energy storage in aqueous electrolytes. *Energy Environ. Sci.* **12**, 1349–1357 (2019).
- Wang, H. et al. Energy storing bricks for stationary PEDOT supercapacitors. *Nat. Commun.* **11**, 3882 (2020).

15. Rivnay, J. et al. Organic electrochemical transistors. *Nat. Rev. Mater.* **3**, 17086 (2018).
16. Pappa, A. M. et al. Direct metabolite detection with an n-type accumulation mode organic electrochemical transistor. *Sci. Adv.* **4**, eaat0911 (2018).
17. van de Burgt, Y. et al. A non-volatile organic electrochemical device as a low-voltage artificial synapse for neuromorphic computing. *Nat. Mater.* **16**, 414–418 (2017).
18. Gkoupidenis, P., Koutsouras, D. A. & Malliaras, G. G. Neuromorphic device architectures with global connectivity through electrolyte gating. *Nat. Commun.* **8**, 15448 (2017).
19. Giovannitti, A. et al. The role of the side chain on the performance of n-type conjugated polymers in aqueous electrolytes. *Chem. Mater.* **30**, 2945–2953 (2018).
20. Bernardis, D. A. & Malliaras, G. G. Steady-state and transient behavior of organic electrochemical transistors. *Adv. Funct. Mater.* **17**, 3538–3544 (2007).
21. Inal, S., Malliaras, G. G. & Rivnay, J. Benchmarking organic mixed conductors. *Nat. Commun.* **8**, 1767 (2017).
22. Khodagholy, D. et al. In vivo recordings of brain activity using organic transistors. *Nat. Commun.* **4**, 1575 (2013).
23. Hallani, R. K. et al. Regiochemistry-driven organic electrochemical transistor performance enhancement in ethylene glycol-functionalized polythiophenes. *J. Am. Chem. Soc.* **143**, 11007–11018 (2021).
24. Ohayon, D. et al. Influence of side chains on the n-type organic electrochemical transistor performance. *ACS Appl. Mater. Interfaces* **13**, 4253–4266 (2021).
25. Maria, I. P. et al. The effect of alkyl spacers on the mixed ionic-electronic conduction properties of n-type polymers. *Adv. Funct. Mater.* **31**, 2008718 (2021).
26. Chen, X. et al. n-Type rigid semiconducting polymers bearing oligo(ethylene glycol) side chains for high-performance organic electrochemical transistors. *Angew. Chem. Int. Ed.* **60**, 9368–9373 (2021).
27. Moser, M. et al. Controlling electrochemically induced volume changes in conjugated polymers by chemical design: from theory to devices. *Adv. Funct. Mater.* **31**, 2100723 (2021).
28. Moser, M. et al. Side chain redistribution as a strategy to boost organic electrochemical transistor performance and stability. *Adv. Mater.* **32**, 1–6 (2020).
29. Kline, R. J., McGehee, M. D., Kadnikova, E. N., Liu, J. & Fréchet, J. M. J. Controlling the field-effect mobility of regioregular polythiophene by changing the molecular weight. *Adv. Mater.* **15**, 1519–1522 (2003).
30. Brinkmann, M. & Rannou, P. Molecular weight dependence of chain packing and semicrystalline structure in oriented films of regioregular poly(3-hexylthiophene) revealed by high-resolution transmission electron microscopy. *Macromolecules* **42**, 1125–1130 (2009).
31. Fratini, S., Nikolka, M., Salleo, A., Schweicher, G. & Sirringhaus, H. Charge transport in high-mobility conjugated polymers and molecular semiconductors. *Nat. Mater.* **19**, 491–502 (2020).
32. Shin, Y. H. et al. Synthesis and aggregation behavior of a glycolated naphthalene diimide bithiophene copolymer for application in low-level n-doped organic thermoelectrics. *Macromolecules* **53**, 5158–5168 (2020).
33. Koch, F. P. V. et al. The impact of molecular weight on microstructure and charge transport in semicrystalline polymer semiconductors—poly(3-hexylthiophene), a model study. *Prog. Polym. Sci.* **38**, 1978–1989 (2013).
34. Gu, K. et al. Assessing the Huang-Brown description of tie chains for charge transport in conjugated polymers. *ACS Macro Lett.* **7**, 1333–1338 (2018).
35. Liu, F. et al. Molecular weight dependence of the morphology in P3HT:PCBM solar cells. *ACS Appl. Mater. Interfaces* **6**, 19876–19887 (2014).
36. Wu, H. et al. Influence of molecular weight on the organic electrochemical transistor performance of ladder-type conjugated polymers. *Adv. Mater.* **34**, 2106235 (2022).
37. Giovannitti, A. et al. N-type organic electrochemical transistors with stability in water. *Nat. Commun.* **7**, 13066 (2016).
38. Maria, I. P. et al. Enhancing the backbone coplanarity of n-type copolymers for higher electron mobility and stability in organic electrochemical transistors. *Chem. Mater.* <https://doi.org/10.1021/ACS.CHEMMATER.2C01552> (2022).
39. Kosco, J. et al. The effect of residual palladium catalyst contamination on the photocatalytic hydrogen evolution activity of conjugated polymers. *Adv. Energy Mater.* **8**, 1802181 (2018).
40. Bracher, C. et al. The effect of residual palladium catalyst on the performance and stability of PCDTBT:PC70BM organic solar cells. *Org. Electron.* **27**, 266–273 (2015).
41. Troshin, P. A. et al. Impedance measurements as a simple tool to control the quality of conjugated polymers designed for photovoltaic applications. *Adv. Funct. Mater.* **20**, 4351–4357 (2010).
42. Shao, M. Palladium-based electrocatalysts for hydrogen oxidation and oxygen reduction reactions. *J. Power Sources* **196**, 2433–2444 (2011).
43. Nielsen, C. B. et al. Molecular design of semiconducting polymers for high-performance organic electrochemical transistors. *J. Am. Chem. Soc.* **138**, 10252–10259 (2016).
44. Liu, J., Loewe, R. S. & McCullough, R. D. Employing MALDI-MS on poly(alkylthiophenes): analysis of molecular weights, molecular weight distributions, end-group structures, and end-group modifications. *Macromolecules* **32**, 5777–5785 (1999).
45. Zhan, C. G., Nichols, J. A. & Dixon, D. A. Ionization potential, electron affinity, electronegativity, hardness, and electron excitation energy: molecular properties from density functional theory orbital energies. *J. Phys. Chem. A* **107**, 4184–4195 (2003).
46. Giovannitti, A. et al. Controlling the mode of operation of organic transistors through side-chain engineering. *Proc. Natl Acad. Sci. USA* **113**, 12017–12022 (2016).
47. Jeong, D. et al. High-performance n-type organic electrochemical transistors enabled by aqueous solution processing of amphiphilicity-driven polymer assembly. *Adv. Funct. Mater.* **32**, 2111950 (2022).
48. Zhang, L. et al. Conjugated polymers based on thiazole flanked naphthalene diimide for unipolar n-type organic field-effect transistors. *Chem. Mater.* **30**, 8343–8351 (2018).
49. Savva, A. et al. Solvent engineering for high-performance n-type organic electrochemical transistors. *Adv. Electron. Mater.* **5**, 1900249 (2019).
50. Noriega, R. et al. A general relationship between disorder, aggregation and charge transport in conjugated polymers. *Nat. Mater.* **12**, 1038–1044 (2013).
51. Brinkmann, M. et al. Segregated versus mixed interchain stacking in highly oriented films of naphthalene diimide bithiophene copolymers. *ACS Nano* **6**, 10319–10326 (2012).
52. Moser, M. et al. Propylene and butylene glycol: new alternatives to ethylene glycol in conjugated polymers for bioelectronic applications. *Mater. Horiz.* **9**, 973–980 (2022).
53. Sachs, M. et al. Tracking charge transfer to residual metal clusters in conjugated polymers for photocatalytic hydrogen evolution. *J. Am. Chem. Soc.* **142**, 14574–14587 (2020).
54. Krebs, F. C., Nyberg, R. B. & Jørgensen, M. Influence of residual catalyst on the properties of conjugated polyphenylenevinylene materials: palladium nanoparticles and poor electrical performance. *Chem. Mater.* **16**, 1313–1318 (2004).

55. Tian, X., Lu, X. F., Xia, B. Y. & Lou, X. W. Advanced electrocatalysts for the oxygen reduction reaction in energy conversion technologies. *Joule* **4**, 45–68 (2020).
56. Michaelson, H. B. The work function of the elements and its periodicity. *J. Appl. Phys.* **48**, 4729–4733 (1977).
57. Gu, D., Dey, S. K. & Majhi, P. Effective work function of Pt, Pd, and Re on atomic layer deposited HfO₂. *Appl. Phys. Lett.* **89**, 082907 (2006).
58. Giovannitti, A. et al. Energetic control of redox-active polymers toward safe organic bioelectronic materials. *Adv. Mater.* **32**, 1908047 (2020).
59. Nikiforov, M. P. et al. Detection and role of trace impurities in high-performance organic solar cells. *Energy Environ. Sci.* **6**, 1513–1520 (2013).
60. Björklund, N. et al. The effects of metal impurities in poly[(2,5-bis(3-decylthiophen-2-yl)thieno[2,3-b]thiophene)] on field-effect transistor properties. *Org. Electron.* **10**, 215–221 (2009).
61. Moser, M. et al. Polaron delocalization in donor–acceptor polymers and its impact on organic electrochemical transistor performance. *Angew. Chem. Int. Ed.* **60**, 7777–7785 (2021).
62. Kim, Y. et al. Strain-engineering induced anisotropic crystallite orientation and maximized carrier mobility for high-performance microfiber-based organic bioelectronic devices. *Adv. Mater.* **33**, 2007550 (2021).
63. Savva, A. et al. Influence of water on the performance of organic electrochemical transistors. *Chem. Mater.* **31**, 927–937 (2019).
64. Szumska, A. A. et al. Reversible electrochemical charging of n-type conjugated polymer electrodes in aqueous electrolytes. *J. Am. Chem. Soc.* **143**, 14795–14805 (2021).
65. Jiang, Z. GIXSGUI: a MATLAB toolbox for grazing-incidence X-ray scattering data visualization and reduction, and indexing of buried three-dimensional periodic nanostructured films. *J. Appl. Crystallogr.* **48**, 917–926 (2015).
66. Bi, X., Crum, B. P. & Li, W. Super hydrophobic parylene-C produced by consecutive O₂ and SF₆ plasma treatment. *J. Microelectromech. Syst.* **23**, 628–635 (2014).

Acknowledgements

S.G., A.M., C.M.A., I.M., D.M., and J.R. acknowledge financial support from KAUST Office of Sponsored Research CRG10. S.G., A.M., C.M.A., and I.M. acknowledge funding by EU Horizon2020 grant agreement no. 952911, BOOSTER, grant agreement no. 862474, RoLA-FLEX, and grant agreement no. 101007084 CITYSOLAR, as well as EPSRC Projects EP/T026219/1 and EP/W017091/1. A CC-BY licence is applied to the AAM arising from this submission, in accordance with the grant's open access conditions. J.R. and E.A.S. gratefully acknowledges funding support from Sloan under award no. FG-2019-12046. B.D.P. and J.R. acknowledge support from the National Science Foundation grant no. NSF DMR-1751308. D.M. and E.A.S. utilized the Keck-II facility of Northwestern University's NUANCE Center and the Northwestern University Micro/Nano Fabrication Facility (NUFAB), which are both partially supported by Soft and Hybrid Nanotechnology Experimental (SHyNE) Resource (NSF ECCS-1542205), the Materials Research Science and Engineering Center (NSF DMR-1720139), the State of Illinois, and Northwestern University. Additionally, the Keck-II facility is partially supported by the International Institute for Nanotechnology (IIN); the Keck Foundation; and the State of Illinois, through the IIN. D.M. and B.D.P. used resources of the Advanced Photon Source, a U.S. Department of Energy (DOE) Office of Science User Facility operated for the DOE Office of Science by Argonne National Laboratory under Contract No. DE-AC02-06CH11357. J.T. acknowledges financial support from a US Office for Naval Research, ONR YIP (N00014-

20-1-2777). Special thanks to J. Strzalka for beam line support. N.B., G.R., and O.B. thank the European Research Council (ERC) for supporting this research by a Starting Grant (No. 714586, OSIRIS) and acknowledge NCCR-MUST, a research instrument of the Swiss National Science Foundation, as well as the University of Bern. M.I.N. and T.D.A. would like to acknowledge the King Abdullah University of Science and Technology (KAUST) Office of Sponsored Research (OSR) under Award No.: OSR-2018-CARF/CCF-3079, and OSR-2019-CRG8-4095 for the funding.

Author contributions

S.G. synthesized the monomers, conducted preparative GPC of the polymers and wrote the manuscript, A.M. synthesized the polymers and performed cyclic voltammetry measurements, D.M. performed OECT characterization, G.R. and O.B. performed UV-Vis spectroscopy and spectroelectrochemical measurements, B.D.P. performed GIWAXS measurements and assisted with the analysis, H.C. performed GPC measurements, K.W. performed ICP-MS measurements and analysis, M.I.N. performed OTFT measurements and analysis, E.A.S. fabricated the OECT substrates and assisted with OECT analysis, J.T. analyzed the GIWAXS data, C.M.A. cowrote the manuscript, T.D.A. led the OTFT measurements, N.B. managed the optical measurements, J.R. managed the OECT and GIWAXS measurements and provided project direction and I.M. managed the project and assisted with writing the manuscript.

Competing interests

The authors declare no competing interests.

Additional information

Supplementary information The online version contains supplementary material available at <https://doi.org/10.1038/s41467-022-35573-y>.

Correspondence and requests for materials should be addressed to Iain McCulloch.

Peer review information *Nature Communications* thanks Ludvig Edman and the other anonymous reviewer(s) for their contribution to the peer review of this work.

Reprints and permissions information is available at <http://www.nature.com/reprints>

Publisher's note Springer Nature remains neutral with regard to jurisdictional claims in published maps and institutional affiliations.

Open Access This article is licensed under a Creative Commons Attribution 4.0 International License, which permits use, sharing, adaptation, distribution and reproduction in any medium or format, as long as you give appropriate credit to the original author(s) and the source, provide a link to the Creative Commons license, and indicate if changes were made. The images or other third party material in this article are included in the article's Creative Commons license, unless indicated otherwise in a credit line to the material. If material is not included in the article's Creative Commons license and your intended use is not permitted by statutory regulation or exceeds the permitted use, you will need to obtain permission directly from the copyright holder. To view a copy of this license, visit <http://creativecommons.org/licenses/by/4.0/>.

© The Author(s) 2022